

Emergent Gravity Fails to Explain Color-dependent Galaxy-Galaxy Lensing Signal from SDSS DR7

Wentao Luo^{1,2}, Jiajun Zhang³, Vitali Halenka⁴, Xiaohu Yang^{5,6}, Surhud More^{7,2}, Christopher J. Miller^{4,8}, Lei Liu⁹, and Feng Shi^{10,11}

² Kavli Institute for the Physics and Mathematics of the Universe (Kavli IPMU, WPI), University of Tokyo, Chiba 277-8582, Japan Center for Theoretical Physics of the Universe, Institute for Basic Science (IBS), Daejeon 34126, Republic of Korea ⁴ Department of Physics, University of Michigan, Ann Arbor, MI 48109, USA

⁷ The Inter-University Center for Astronomy and Astrophysics, Post bag 4, Ganeshkhind, Pune, 411007, India

Department of Astronomy, University of Michigan, Ann Arbor, MI 48109, USA

Shanghai Astronomical Observatory, Shanghai 200030, People's Republic of China

Abstract

We test Verlinde's Emergent Gravity (EG) theory using a galaxy-galaxy lensing technique based on Sloan Digital Sky Survey DR7 data. In the EG scenario, we do not expect a color dependence of the galaxy sample in the apparent dark matter predicted by EG, which is exerted only by the baryonic mass. If the baryonic mass is similar, then the predicted lensing profiles from the baryonic mass should be similar according to EG, regardless of the color of the galaxy sample. We use the stellar mass of the galaxy as a proxy of its baryonic mass. We divide our galaxy sample into five stellar mass bins, and further classify them as red and blue subsamples in each stellar mass bin. If we set the halo mass and concentration as free parameters, ΛCDM is favored by our data in terms of the reduced χ^2 , while EG fails to explain the color dependence of the excess surface density from the galaxy–galaxy lensing measurement.

Unified Astronomy Thesaurus concepts: Quantum gravity (1314); Weak gravitational lensing (1797)

1. Introduction

Today, the concordance cosmological model where dark matter and dark energy form about 95% of the energy density of the universe is supported by a plethora of observations including those of the cosmic microwave background (CMB; see, e.g., Planck Collaboration et al. 2016), supernovae of Type Ia (see, e.g., Perlmutter et al. 1999), baryon acoustic oscillations (BAO; see, e.g., Eisenstein et al. 2005), as well as weak lensing (see, e.g., Heymans et al. 2012; Kuijken et al. 2015; Shi et al. 2018). The observational data from the above probes can be described by merely half a dozen major parameters, a.k.a ΛCDM, despite a recent claim of 5.3σ tension in H_0 between the CMB probe (Planck Collaboration et al. 2020) and thee strong lensing time delay project H0LiCOW (Wong et al. 2020) and the SH0ES (SNe, H_0 , for the Equation of State of dark energy) project (Riess et al. 2016). Regardless of this success, dark matter still remains a mystery.

The concept of dark matter was first introduced by Zwicky (1937) based on the anomalous dynamics of galaxies in clusters, which required excess gravitational influence than that from the baryonic component only. Observations of galaxy rotation curves (Bosma 1981; Sofue & Rubin 2001) further confirm this anomalous behavior. These observations require the presence of dark matter that cannot be detected in any electromagnetic observations that dominate the matter sector of the universe. Since then, the study of the properties of dark matter has become one of the frontier fields from both a particle physics perspective and the modified gravity scenario.

There are plenty of models from particle physics and possible detection experiments in the literature ranging from the light boson model (e.g., axion dark matter, which arises from the Peccei-Quinn solution; Duffy 2009) to the strong charge-conjugation parity problem (sterile neutrino as potential candidate; Kisslinger & Das 2019) and weakly interacting massive particles predicted by R-parity-conserving supersymmetry (Jungman et al. 1996). And so far, there are no experiments that can confirm any of the models, neither Earthbased labs (Kang et al. 2010; Aprile et al. 2019; Zhang et al. 2019) nor space-based detection (Ding et al. 2019; Di Mauro et al. 2020).

On the other hand, some researchers try to view dark matter as the modification of the theory of gravity. For example, MOdified Newtonian Dynamics (MOND; Milgrom 1983, 2011, 2020) explains the high speed stars in galaxies by adding an interpolation function to modify the acceleration of Newtonian theory. Bekenstein (2004) further improves MOND by considering gravity as a mixture of dynamics of metric, a scalar, and a four-vector field, a.k.a TeVes, which can predict consistent weak lensing signals. Milgrom (2013) claims that the MOND prediction agrees with the velocity dispersion to the *r*-band luminosity relation $\sigma - L_r(h^{-2}L_\odot)$ based on the Canada–France– Hawaii Telescope (CFHT) data (Heymans et al. 2013), but without comparison of the galaxy-galaxy lensing profiles directly as in Brouwer et al. (2017). Chae et al. (2020) find evidence that supports MOND gravity from the observations of Spitzer Photometry and Accurate Rotation Curves (SPARC).

¹ CAS Key Laboratory for Research in Galaxies and Cosmology, University of Science and Technology of China, Hefei, Anhui 230026, People's Republic of China wentao.luo82@gmail.com

⁵ Department of Astronomy, School of Physics and Astronomy, and Shanghai Key Laboratory for Particle Physics and Cosmology, Shanghai Jiao Tong University, Shanghai, 200240, People's Republic of China

⁶ Tsung-Dao Lee Institute, and Key Laboratory for Particle Physics, Astrophysics and Cosmology, Ministry of Education, Shanghai Jiao Tong University, Shanghai, 200240, People's Republic of China

School of Aerospace Science and Technology, Xidian University, 266 Xinglong Section of Xifeng Road, Xi'an, Shaanxi 710126, People's Republic of China Korea Astronomy and Space Science Institute, 776 Daedeok-daero, Yuseong-gu, Daejeon 34055, Republic of Korea Received 2020 April 6; revised 2021 March 18; accepted 2021 April 1; published 2021 June 18

Among the various MOND models, there is a unique one based on an entropic scenario. Verlinde (2017) reconsidered the gravity as the underlying microscopic description inspired by the laws of black hole thermodynamics (Bardeen et al. 1973; i.e., Emergent Gravity; EG). Brouwer et al. (2017) first tested this assumption using the galaxy–galaxy lensing technique based on the data from Kilo Degree Survey (KiDS; de Jong et al. 2013) and the Galaxy and Mass Assembly (GAMA; Driver et al. 2009); they claimed that both the dark-matter scenario and EG can fit the galaxy–galaxy lensing signal equally well.

ZuHone & Sims (2019) tested EG using relaxed galaxy clusters and found that the inclusion of the central galaxy improves the agreement between observations and the theory in the inner regions ($r \le 30$ kpc). On larger scales, the predictions are discrepant with observations and Λ CDM models fit the observations better. However, Halenka & Miller (2020) found that there is enough freedom in the EG theory for it to agree with the data as well as Λ CDM, especially after accounting for possible observational systematics. Baryonic physics complicate the inference of the underlying gas density profile and weaken the constraining power of the observations.

In this paper, we retest this theory by using much larger survey data from the Sloan Digital Sky Survey (SDSS) DR7 (Abazajian et al. 2009) as well as two cosmology models in ΛCDM framework, i.e., WMAP5 (Komatsu et al. 2009) and PLANCK18 (Planck Collaboration et al. 2020). We minimize the complicated modeling of massive clusters by only selecting single-galaxy systems from the Yang et al. (2007) catalog with a mean halo mass of $\log M \leq 13.5h^{-1}M_{\odot}$. None of the systems have X-ray detection, which further minimizes the hot baryonic contribution. With this data set, we are able to select isolated galaxies. Our sample is at least five times bigger than that used in Brouwer et al. (2017) as we use the group catalog built by Yang et al. (2007). The models of the galaxy-galaxy lensing signals from both EG and Λ CDM are described in Section 2. We introduce the lensing data and methodology in Section 3. The results are given in Section 4. Finally, we summarize and discuss in Section 5.

2. The Galaxy-Galaxy Lensing Models

2.1. The Lensing Model in Emergent Gravity

The tangential distortions of background galaxy shapes caused by weak gravitational lensing are proportional to the excess surface density (ESD), $\Delta\Sigma$, which is the difference in the average surface density within a projected radius R and the surface density at radius R. The ESD is related to the tangential shear $\gamma_l(R)$ by a factor Σ_c ,

$$\gamma_t(R)\Sigma_c = \Delta\Sigma(R) = \Sigma(\leqslant R) - \Sigma(R),$$
 (1)

where Σ_c is the critical density dependent upon the geometric distances between the observer, lens, and source galaxy. For the Λ CDM case, we refer to Yang et al. (2006) for detailed formulation, which is well established in galaxy–galaxy lensing studies.

In the Emergent Gravity (hereafter EG) scenario, a term additional to the normal baryonic mass arises that can act as an apparent dark-matter contribution. Based on Verlinde (2017), the extra term of the gravitational potential is exerted by the entropy displacement from total galaxy mass $M_g(r)$, where M(r) is the mass enclosed within a radius r. This mass includes

stellar mass and cold gas components. As a result, the apparent mass $M_o(r)$ is related to $M_o(r)$ via

$$M_a^2(r) = \frac{cH_0r^2}{6G} \frac{d[M_g(r)r]}{dr}.$$
 (2)

As in Brouwer et al. (2017), for a typical mass of $M = 10^{10}h^{-2}M_{\odot}$, EG becomes significant over a scale larger than $2 h^{-1}$ kpc. We measure our galaxy–galaxy lensing signal from $0.01 h^{-1}$ Mpc all the way to $1 h^{-1}$ Mpc to empirically test the scale dependence of both theories. We follow Brouwer et al. (2017) that beyond $30 h^{-1}$ kpc the galaxy can be considered a point mass. We exclude the first data point within $30 h^{-1}$ kpc. In Section 4, we calculate the χ^2 excluding the first data point of each of the measurements below this scale.

From Equation (2), we get the mass distribution

$$M_a(r) = \left[\frac{cH_0r^2}{6G} \left(M_g(r) + r \frac{\partial M_g(r)}{\partial r} \right) \right]^{0.5}$$

and the second term on the right side is gone under the point mass assumption, i.e., $M_g(r) = M_g$, and we can treat the factor $\sqrt{\frac{cH_0}{6G}}$ as a combined constant C_a , also following Brouwer et al. (2017). The density profile can be related to the derivative of the mass distribution

$$\rho_{\rm EG}(r) = \frac{1}{4\pi r^2} \frac{dM_a(r)}{dr} = \frac{C_a \sqrt{M_g}}{4\pi r^2}.$$
 (3)

The 2D surface density at projected distance R is then bearing the form

$$\Sigma_{\rm EG}(R) = \int_{-\infty}^{\infty} \rho_{\rm EG}(R, \chi) d\chi = \frac{C_a \sqrt{M_g}}{4R},\tag{4}$$

where $r^2 = R^2 + \chi^2$ with R as the projected distance and χ as the distance along the line of sight. Then the ESD of the EG point mass can be calculated as

$$\Delta\Sigma_{\rm EG}(R) = \frac{C_a \sqrt{M_g}}{4R},\tag{5}$$

which happens to be the same as Equation (4). Together with the original baryonic mass contribution, the total ESD profile as predicted by EG is

$$\Delta\Sigma(R)_{\rm all} = \frac{M_g}{\pi R^2} + \Delta\Sigma_{\rm EG}(R). \tag{6}$$

In the Λ CDM scenario, the dark-matter density profile can be accurately described by an Navarro–Frenk–White (NFW) profile (Navarro et al. 1997). When converting the 3D NFW profile to the 2D ESD, it differs from the EG profile.

2.2. The Lensing Model in ΛCDM

We model the ESD based on the NFW density profile with two free parameters, namely halo mass and concentration parameters, and we label this model as "NFW." We use the Yang et al. (2006) formulation to model the ESD given a halo mass based on an NFW dark-matter halo profile (Navarro et al. 1997),

$$\rho(r) = \frac{\rho_0}{(r/r_s)(1 + r/r_s)^2},\tag{7}$$

with $\rho_0 = \frac{\bar{\rho}\Delta_{\rm vir}}{3I}$, where $\Delta_{\rm vir} = 200$, $I = \frac{1}{c^3} \int_0^c \frac{x dx}{(1+x)^2}$. Here c is the concentration parameter defined as the ratio between the virial radius of a halo and its characteristic scale radius r_s .

Recently, the group catalog was also updated to include an abundance-matching-based halo mass estimation in both the WMAP5 and PLANCK18 cosmology. We will therefore further examine the cosmology dependence.

In the Λ CDM scenario, the ESD is composed of the following simple two components: the host halo mass and the stellar mass,

$$\Delta\Sigma(R) = \Delta\Sigma_{\text{host}}(R) + \Delta\Sigma_{*}.$$
 (8)

We do not include two-halo term, which is the signal caused by the large-scale structure due to the fact that we select the isolated galaxies and we only measure our signal to $1\,h^{-1}$ Mpc. The contribution of the stellar components from the lens galaxy can be modeled as a point mass of

$$\Delta\Sigma_*(R) = \frac{M_*}{\pi R^2}. (9)$$

 $\Delta\Sigma_{\rm host}$ is the contribution of the halo given that the galaxy is perfectly located at the center.

3. The Galaxy-Galaxy Lensing Signals

In this section, we describe the data we use to measure the galaxy-galaxy lensing signals.

3.1. Lenses

The lenses are selected from the galaxy group catalog constructed from the spectroscopic SDSS survey (DR7; Yang et al. 2007), which is based on a halo-based group finding algorithm (Yang et al. 2005). Recently, Yang et al. (2021) extended this group finder so that it can deal with galaxies with photometric and spectroscopic redshifts simultaneously, and successfully applied it to the Dark Energy Spectroscopic Instrument (DESI) Legacy surveys data release 8 (Dey et al. 2019). The strength of this algorithm is related with its iteration nature and the application of an adaptive filter according to the general properties of the dark-matter halos. It starts with assuming that each galaxy is a potential group candidate and then calculates the total luminosity of each system. The halo mass is then estimated based on abundance matching. After the halo mass estimation, the other quantities such as velocity dispersion, virial radius, etc., are then deduced. The member galaxies are determined by selecting galaxies that meet the criteria, which include distance and redshift information. All the above procedures are iterated several times until the massto-light ratios converge. There are systems with only one central galaxy, meaning that there are no other galaxies brighter than the magnitude limit r = 17.77 within the projected virial radius and with $\Delta z = |z_i - z_{\text{group}}|$ less than the viral velocity of the dark-matter halo along the line-of-sight direction.

In total, there are $472,\overline{4}19$ groups in the sample. In order to minimize the effects of nearby structures, we only select single-galaxy systems which further reduces the number to 400,608. The stellar mass of each galaxy is computed using a stellar mass-to-light ratio and color from Bell et al. (2003), but with a Kroupa initial mass function (IMF; Kroupa 2001). This leads to a -0.1 correction to the stellar mass-to-light ratio relation. The statistical scatter of the color-based stellar ML ratio is about 20%. Systematics rising from galaxy age, dust, and bursts of

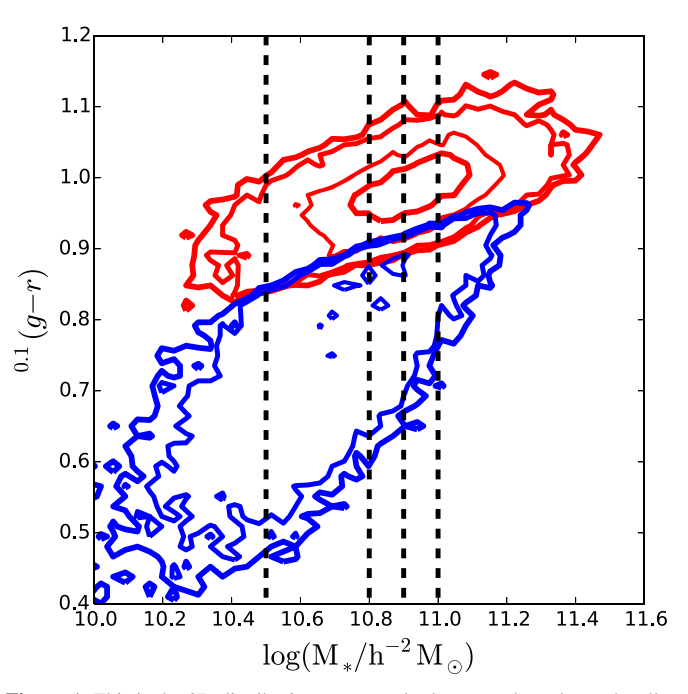


Figure 1. This is the 2D distribution contour plot between the color and stellar mass of the lens galaxy sample. The dashed vertical lines divide the plot into five stellar mass regions, where each region is further divided into red and blue subsamples. The overlap region between the blue and red are due to the fact that the threshold is calculated using color and *r*-band magnitude rather than stellar mass

star formation in total contribute \sim 0.1 dex scatter. In general, the scatter may induce some Eddington bias to the average stellar mass of the galaxies. However, since the total amount of scatter is quite small, the overall Eddington bias can only lead to a \sim 0.03 dex overestimation of stellar mass, which will not impact any of our results significantly.

The sample is subdivided into different stellar mass bins following Brouwer et al. (2017). We add one more stellar mass bin compared to their study, with $\log M_{\rm st}$ mass $\geqslant 11.0$ due to the larger sample size. The mean redshift of our sample is lower than Brouwer et al. (2017), so our work is complementary to theirs as low z test and it provides better agreement with a small redshift assumption of the EG model. Moreover, our samples are at least five times larger to improve the measurement.

The vertical dashed lines in Figure 1 divide our sample in $5 M_*$ bins. We further subdivide our sample of galaxies in to blue star-forming galaxies and red passive galaxies based on a cut in the color-magnitude plane from Yang et al. (2008) such that

$$^{0.1}(g-r) = 1.022 - 0.0652x - 0.0031x^2,$$
 (10)

where $x = {}^{0.1} M_r - 5 \log h + 23.0$, and ${}^{0.1} M_r - 5 \log h$ is the absolute magnitude of galaxy after K correction and evolution correction to a redshift of z = 0.1. The statistics of the our subsamples is given in Table 1 and is illustrated in Figure 1. The overlap between the red and blue contours are due to the fact that threshold in Equation (10) is calculated based on color and magnitude, while Figure 1 is the color and stellar mass 2D distribution.

We treat the gas contribution following that in Brouwer et al. (2017) and Boselli et al. (2014) for the blue galaxies, which applies a factor $f_{\rm cold}$ so that the total galaxy mass M_g can be

 Table 1

 Properties of the Lens Samples Created for This Paper

log M _{st} Range	Num	⟨ z ⟩	$\langle \log(M_{\rm st}/h^{-2}M_{\odot})\rangle$	$\log(Mh_{W5}/h^{-1}M_{\odot})$	$\log(Mh_{PL}/h^{-1}M_{\odot})$
8.5-10.5	216 212	0.078	10.001	$11.563^{+0.059}_{-0.062}$	11.686 ^{+0.063} _{-0.069}
RED	69 914	0.074	10.180	$11.861^{+0.067}_{-0.073}$	$11.983^{+0.070}_{-0.076}$
BLUE	146 298	0.079	9.916	$11.354^{+0.099}_{-0.112}$	$11.378^{+0.099}_{-0.113}$
10.5-10.8	104 484	0.123	10.648	$11.935^{+0.085}_{-0.087}$	$12.210^{+0.072}_{-0.077}$
RED	61 278	0.115	10.654	$12.086^{+0.108}_{-0.108}$	$12.284^{+0.089}_{-0.093}$
BLUE	43 206	0.134	10.640	$11.761^{+0.149}_{-0.187}$	$11.758^{+0.161}_{-0.207}$
10.8-10.9	28 747	0.143	10.848	$12.493^{+0.121}_{-0.119}$	$12.725^{+0.103}_{-0.105}$
RED	19 735	0.140	10.849	$12.566^{+0.108}_{-0.108}$	$12.810^{+0.104}_{-0.107}$
BLUE	9 012	0.151	10.847	$12.346^{+0.367}_{-0.546}$	$12.312^{+0.399}_{-0.585}$
10.9-11.0	22 330	0.155	10.946	$12.449^{+0.189}_{-0.225}$	$12.596^{+0.220}_{-0.247}$
RED	16 965	0.155	10.948	$12.516^{+0.187}_{-0.218}$	$12.948^{+0.465}_{-0.569}$
BLUE	5 365	0.156	10.944	$12.218^{+0.506}_{-0.690}$	$12.601^{+0.228}_{-0.271}$
11.0-above	24 717	0.165	11.087	$12.673^{+0.104}_{-0.102}$	$13.000^{+0.075}_{-0.083}$
RED	20 584	0.166	11.119	$12.733^{+0.106}_{-0.103}$	$13.075^{+0.081}_{-0.086}$
BLUE	4 133	0.158	11.096	$12.155^{+0.411}_{-0.578}$	$12.426^{+0.384}_{-0.656}$

Note. $\log(Mh_{W5}/h^{-1}M_{\odot})$ and $\log(Mh_{P18}/h^{-1}M_{\odot})$ are the weak lensing fitted mass for the two different cosmologies.

written as

$$M_g = M_*(1 + f_{\text{cold}}).$$
 (11)

Boselli et al. (2014) give an empirical form of f_{cold} based on Herschel Reference Survey (Boselli et al. 2010),

$$\log(f_{\text{cold}}) = -0.69 \log(M_*/h^{-2}M_{\odot}) + 6.63.$$
 (12)

For the red galaxy, we apply a constant fraction of 1%, which is the upper limit from Boselli et al. (2014) for early-type galaxies. We do not take the hot gas into consideration so far because first, the dominant factor is stellar mass, as in Brouwer et al. (2017), as we focus on the point mass contribution by selecting single-galaxy system, and the hot gas contribution is less than the 0.1 dex systematic for the stellar mass estimation.

We also add the fitted NFW halo mass for each sample with errors in Section 4.

3.2. Sources and Estimator

For the source catalog, we use the shape catalog created by Luo et al. (2017) based on the SDSS DR7 imaging data. The DR7 imaging data, with the u, g, r, i, and z bands, covers about 8423 square degrees of the SDSS Legacy Survey sky (\sim 230 million distinct photometric objects). The total number of objects identified as galaxies is around 150 million. The final shape catalog for our study contains about 40 million galaxies with position, shape, shape error, and photoZ information based on Csabai et al. (2007), which fits a local color–color hyperplane with the nearest 100 objects.

The shear signals $\Delta\Sigma(R)$ can be measured by the weighted mean of source galaxy shapes,

$$\Delta\Sigma(R) = \frac{1}{2\bar{R}} \frac{\sum w_i e_t(R) \sum_{\text{cls}}}{\sum w_i},$$
(13)

where w_i is the weight for each source galaxy. $\Sigma_{\rm cls} = \frac{c^2}{4\pi G} \frac{D_{\rm s}}{D_{\rm ls} D_l (1+z_l)^2}$ is the critical density for each lens–source pair. We measure the signal in six equal logarithm bins in a projected comoving distance from 0.01 Mpc h^{-1} to 1 Mpc h^{-1} . The weighting term is composed by shape noise $\sigma_{\rm shape}$ and that

from sky $\sigma_{\rm sky}$,

$$w = \frac{1}{(\sigma_{\text{sky}}^2 + \sigma_{\text{shape}}^2)\Sigma_{\text{cls}}^2}.$$
 (14)

We correct the dilution effect by calculating the boost factor, which is from the contamination of nonlensed galaxies due to inaccurate photometric redshift

$$B(R) = \frac{N_{\text{rand}}}{N_{\text{lens}}} \frac{\sum_{i}^{N_{\text{lens}}} w_{\text{ls}}}{\sum_{i}^{N_{\text{rand}}} w_{\text{rs}}}.$$
 (15)

 $N_{\rm lens}$ and $N_{\rm rand}$ are the number of lens galaxies of each sample and the corresponding random sample. The weights $w_{\rm ls}(w_{\rm rs})$ correspond to each lens (random position, $N({\rm zrand}) = N({\rm zlens})$) as in Equation (14). The χ^2 can be calculated as

$$\chi^2 = ((\text{data} - \text{model})^{\text{T}} C^{-1}(\text{data} - \text{model})), \tag{16}$$

where C^{-1} is the inverse covariance matrix. We further add the photometric redshift systematic from the weak lensing measurement to the trace of the covariance matrix when we calculate the χ^2 . We estimated the systematics caused by photometric redshift to be 2.7% (Luo et al. 2017) for the most massive stellar mass bin.

4. Results

In this section, we describe the results from the comparison between the EG and Λ CDM model. Our use of a larger data set allows us to obtain a high signal-to-noise ratio (S/N) measurement of galaxy–galaxy lensing signals even after we split the sample into red and blue lens samples to study the color dependence. The S/N is ranging from 17.6 for the blue galaxy sample to 28.1 for red galaxy sample based on Equation (5) in Leauthaud et al. (2017).

Figure 2 is the comparison between the data and different models, i.e., NFW (Mh and c as free parameters) and EG. It is well known that the lensing signal is dependent on several cosmological parameters, e.g., Ω_m , σ_8 , and the Hubble parameter, whereas EG depends only on a Hubble parameter as shown in Equation (2). That is why EG shows stronger

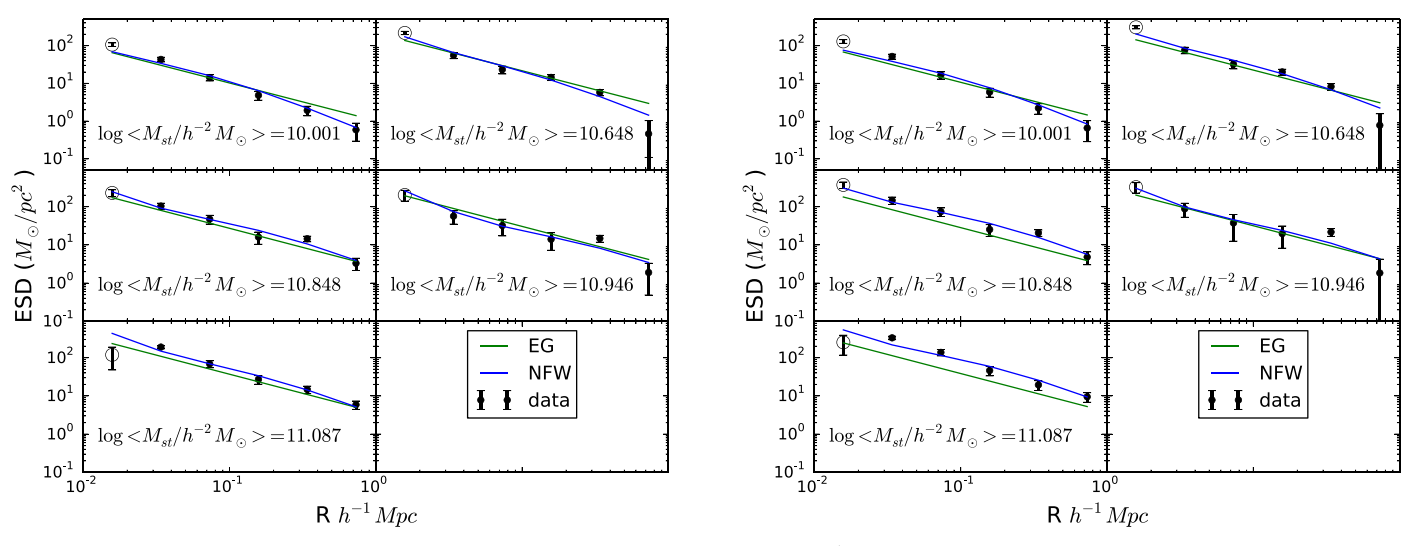


Figure 2. Left: the prediction of the emergent gravity is shown in green and the prediction of the Λ CDM model is shown in blue with PLANCK18, comparing to the weak lensing signal which is shown by the black dots with error bars. Right: same as the left, but with WMAP5 cosmology. The excluded data points in our analysis are shown as empty circles at a scale smaller than $30 \ h^{-1}$ kpc.

Cosmology	NFW $(\chi^2/\text{dof}_{=15})$	$EG(\chi^2/dof_{=25})$
WMAP5	0.949(1.453)	2.959(3.739)
RED	0.717(1.433)	1.851(3.397)
BLUE	0.731(0.682)	2.441(2.085)
PLANCK18	0.868(0.966)	1.907(1.770)
RED	0.718(0.885)	1.792(1.762)
BLUE	0.659(0.626)	2.730(2.391)

Note. The χ^2 values in the parenthesis are calculated by including the first data points from the measurements.

cosmology variance than Λ CDM in terms of reduced χ^2 . Apparently, EG prefers PLANCK18 cosmology with reduced $\chi^2=1.907$ to WMAP5 (reduced $\chi^2=2.959$), as in Table 2. We exclude the first data points from all measurements because it is below 30 kpc h^{-1} , but still show the χ^2 in Table 2 (inside the parenthesis) by including the first data points to see the difference

Our measurement at small stellar mass bins have very high S/Ns. And due to the selection of isolated systems, we have less contribution from an adjacent structure. Therefore, the decreasing feature in the first two stellar mass bins plays an important role to the whole χ^2 . We do not use the extended model as in Brouwer et al. (2017) because the extended model only makes the χ^2 larger.

We show the color dependence in PLANCK18 cosmology in Figure 3. The NFW model with free halo mass and concentration apparently is favored by the data, especially the blue data. Figure 3 shows the ESD profile from the first three stellar mass bins in PLANCK18 cosmology. Due to larger S/N, the rest of two ESD profiles from the massive stellar mass bins do not carry so much information.

In the left panel of Figure 3, there is significant difference between the ESDs from the red and blue lenses. The ESD from the red lens is larger than their blue counterpart with a 0.164 dex difference in the stellar mass but a 0.605 dex difference in the halo mass in the PLANCK18 cosmology. The

stellar mass difference shrinks to 0.014 dex, but the halo mass difference is 0.526 dex for the second stellar mass bin sample. The third stellar mass bin sample has almost identical stellar mass for blue and red galaxies, but the halo mass difference is still up to 0.498 dex.

When comparing to the halo masses directly provided in the group catalog, the first three stellar mass bins have a consistent halo mass estimation for the whole sample after considering a 0.07 Eddington bias, estimated from Luo et al. (2018). The last two show significant discrepancies with the abundancematching halo mass, with a 0.5 dex difference in the last stellar mass bin. We attribute this to the selection effect that we only select a single-galaxy system. Figure 4 shows the stellarmass-to-halo mass relation (SHMR) of our measurement. Our measurement agrees well with both observational calibrations (Leauthaud et al. 2017) and simulation calibrations (Girelli et al. 2020), except for the most massive stellar mass bin. That is due to our simple NFW model and the selection of a singlegalaxy system. The multigalaxy systems in stellar mass bin 4 is about 20.3%, and 33.4% for stellar mass bin 5. We recalculate the multigalaxy sample halo mass for those two bins in PLANCK18 cosmology and obtain a higher halo mass than the single systems in the same stellar mass bin, which are 12.873 and 13.533, respectively. If we simply take the weighted average halo mass together with single systems, we get $12.654 \pm 0.23 \, dex$ and $13.178 \pm 0.08 \, dex$, versus 12.985 and 13.299 from abundance matching.

We also further test the possible contribution of faint satellites out of the SDSS spectroscopic detection limit at an r-band model magnitude of 17.77 around the massive stellar mass bins, based on illustrisTNG300-3 (Nelson et al. 2018) low-resolution hydrosimulation. IllustrisTNG300-3 has 100 snapshots from z at 127, with a 302.6 h^{-1} Mpc box size, a dark-matter particle mass of $3.8 \times 10^9 \, M_\odot$ and a gas stellar cell mass of $7.0 \times 10^8 \, M_\odot$. We downloaded a group catalog from snapshot 91 at z=0.1 as well as processed offset files to obtain the information of dark matter and gas, stellar particles for each halo, and its subhalo. We select four samples based on the halo mass (weak lensing mass \pm error) and stellar mass from Table 1. The stellar particles inside 100 kpc with respect to the centroids of the stacked dark-matter particles are considered to be from the

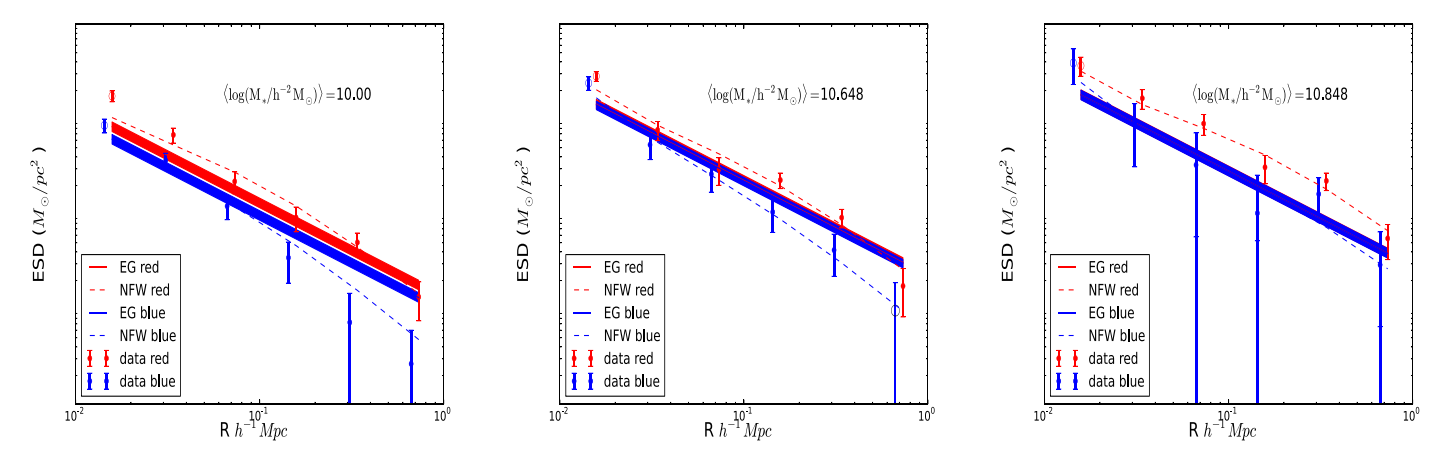


Figure 3. From left to right, these are the plots of stellar mass bins 1, 2, and 3 based on PLANCK18 cosmology. The red and blue dots are the measurements from red and blue galaxy samples. We exclude the first data points within $30 h^{-1}$ kpc, shown as empty circles. The empty circle at the large scale in the middle panel denotes a negative value. The red and blue solid lines are the EG models and the dashed lines are from NFW model. The bandwidth from the EG model is due to the 0.1 dex systematic from the stellar mass estimation based on the method of Bell et al. (2003).

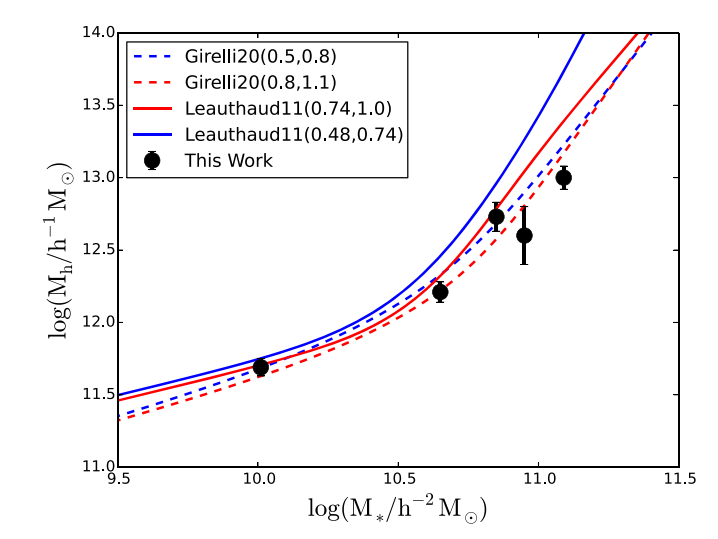


Figure 4. SHMR in our study. Notice that we select single-system groups. So at the massive end, it is not consistent with the theoretical curve due to this selection. And the modeling is simply based on an NFW and stellar mass with a fixed stellar mass contribution.

central galaxies. This criteria is based on the 50 kpc off-center effect (Luo et al. 2017) and the 50 kpc galaxy size from Chen et al. (2020). The ratio between the stellar particles outside this radius and the ones inside this radius is the rough estimation of the contribution of satellite galaxies in general. Figure 5 is an example of a halo from the simulation defined by rockstar software (Behroozi et al. 2013), the black dots are the darkmatter particles, the red dots are the stellar particles, and the boundary of the halo is not regular but roughly about the virial radius of a halo. We find 10% for the most massive stellar mass bin, and this dramatically decreases to 1.0% for the second most massive stellar mass bin. This dramatic decrease may be due to the resolution of the suit of simulations we used here. However, we still can consider the 10% as an upper limit for the satellite contribution. Further more, in observational data, the secondary satellite is beyond 17.77 in the r band, so in reality this is less than 10%. And the contribution for the rest can be neglected. So the unobserved faint galaxies do not contribute significantly to the EG in our analysis.

About 5.7% galaxies (36,759) in the sample are brighter than the r band (17.77), but without spectroscopic redshift

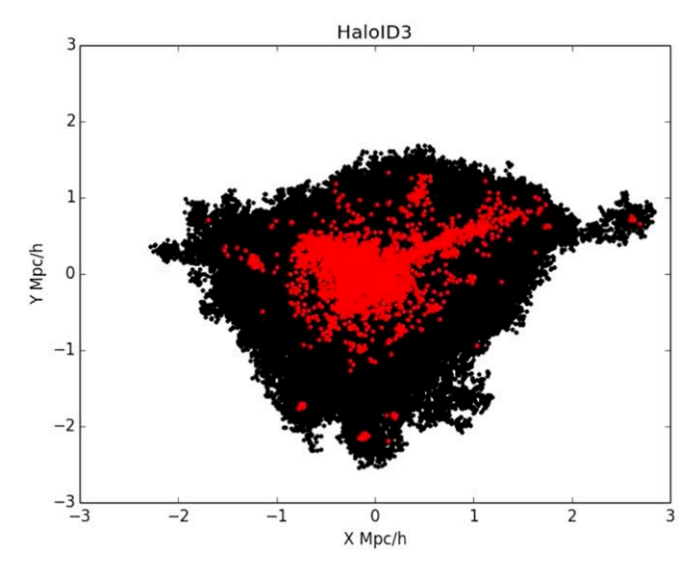


Figure 5. An example of a halo from the simulation. The black dots are the dark-matter particles and the red ones are the stellar components. The radius is not regular due to the shape of the halo defined by *rockstar* software.

measurements due to the fiber-collision effect. According to Zehavi et al. (2002), roughly 60% of the fiber-collision galaxies have a redshift within 500 km s⁻¹. In Yang et al. (2007), they assign a redshift of their nearest neighbors in the group finding procedure. As a result, the single system does not have a close companion with fiber-collision galaxies, therefore our results are not effected by the fiber-collision effect.

In a word, our results are robust against potential influence from either fiber-collision galaxies and faint galaxies with an *r*-band magnitude fainter than 17.77.

5. Summary and Discussion

We select isolated galaxy systems from the SDSS DR7 group catalog (Yang et al. 2007), with recent updated halo mass estimations. This update doubles the number of lens galaxies at small stellar mass bins compared to the sample used in Chen et al. (2020), which enables us to measure high S/N ESD for those samples (17.6 for the blue galaxy sample and 28.1 for the red galaxy sample). Further more, we split each

stellar mass sample into blue and red to test the color dependence.

We model the ESD profile with NFW profiles, setting halo mass and concentration as free parameters based on two cosmologies, i.e., WMAP5 and PLANCK18. The most significant difference is from the ESD between the red and blue lens samples. The ESDs from the blue samples in the same stellar mass bin have lower amplitude than their red counterparts, indicating a smaller halo mass, as apparent dark-matter ESD in the EG framework remains the same as long as the stellar mass is the same. This can be clearly seen in stellar mass bin 2 and 3 where the stellar mass has only 0.014 to 0.002 dex of a difference, while the halo masses have up to a 5σ difference.

We also further test the validity of our selection of isolated systems using illustrisTNG300-3 (Nelson et al. 2018), and we found that the contribution of a possible satellite out of the SDSS spectroscopic detection limit is 10% for the most massive stellar mass bin and 1% for the second most massive stellar mass bin. This effect can be neglected for the rest of the samples.

In general, the EG scenario of gravity failed to explain the color dependence of the galaxy-galaxy lensing signal and we summarize as follows.

- 1. The EG favors PLANCK18 cosmology with reduced $\chi^2_{\rm reduced}=1.907$ to WMAP5 $\chi^2_{\rm reduced}=2.959$ with degrees of freedom of 15 for NFW and 25 for EG. The NFW model shows significantly lower reduced χ^2 values than those from EG already without red and blue dichotomy, which are 0.868(0.996) for the WMAP5 cosmology and 0.949(1.453). The values in the parenthesis are calculated with the first data points from the measurement.
- 2. The most significant difference is from the first three stellar mass bins after the red and blue classification. For instance, in PLANCK18 cosmology the reduced χ^2 is 0.718(0.885) for the red lens sample and 0.659(0.626) for the blue sample, and these values are increased to 1.792 (1.762) and 2.730(2.931), respectively, in EG model.
- 3. The halo mass discrepancy between abundance matching and the NFW model fitting is significant for the last two stellar mass bins; this is due to the combination of the selection effect and the abundance-matching method.
- 4. Our results are consistent with Zu & Mandelbaum (2016) in that the halo masses of blue galaxies in the same stellar mass bins are smaller than that of red galaxies.

We are grateful to Prof. Y. F. Cai, X. Kong, and H. Y. Wang from USTC and Prof. D. C. Dai from YZU, for valuable comments. W.L. acknowledges the support from WPI Japan. All numerics are operated on the computer clusters gfarm at Kavli IPMU and cluster from Shanghai Astronomical Observatory. J.Z. is supported by IBS under the project code IBS-R018-D1. X.Y. is supported by the National Science Foundation of China (NSFC, grant Nos. 11890692, 11833005, and 11621303) and the 111 project No. B20019. C.J.M. was partially supported by the U.S. National Science Foundation under grant No. 1812739. L.L. is supported by the National Science Foundation of China (NSFC, grant No. 11903067).

ORCID iDs

Wentao Luo https://orcid.org/0000-0003-1297-6142
Jiajun Zhang https://orcid.org/0000-0002-4117-343X
Vitali Halenka https://orcid.org/0000-0001-7483-0945
Xiaohu Yang https://orcid.org/0000-0003-3997-4606
Surhud More https://orcid.org/0000-0002-2986-2371
Lei Liu https://orcid.org/0000-0002-2920-1880
Feng Shi https://orcid.org/0000-0002-9968-2894

```
References
Abazajian, K. N., Adelman-McCarthy, J. K., Agüeros, M. A., et al. 2009,
       S, 182, 543
Aprile, E., Aalbers, J., Agostini, F., et al. 2019, PhRvL, 123, 251801
Bardeen, J. M., Carter, B., & Hawking, S. W. 1973, CMaPh, 31, 161
Behroozi, P. S., Wechsler, R. H., & Wu, H.-Y. 2013, ApJ, 762, 109
Bekenstein, J. D. 2004, PhRvD, 70, 083509
Bell, E. F., McIntosh, D. H., Katz, N., & Weinberg, M. D. 2003, ApJS,
  149, 289
Boselli, A., Ciesla, L., Buat, V., et al. 2010, A&A, 518, L61
Boselli, A., Cortese, L., Boquien, M., et al. 2014, A&A, 564, A67
Bosma, A. 1981, AJ, 86, 1791
Brouwer, M. M., Visser, M. R., Dvornik, A., et al. 2017, MNRAS, 466, 2547
Chae, K.-H., Lelli, F., Desmond, H., et al. 2020, ApJ, 904, 51
Chen, Z., Luo, W., Cai, Y.-F., & Saridakis, E. N. 2020, PhRvD, 102, 104044
Csabai, I., Dobos, L., Trencséni, M., et al. 2007, AN, 328, 852
de Jong, J. T. A., Verdoes Kleijn, G. A., Kuijken, K. H., & Valentijn, E. A.
  2013, ExA, 35, 25
Dey, A., Schlegel, D. J., Lang, D., et al. 2019, AJ, 157, 168
Di Mauro, M., Stref, M., & Calore, F. 2020, PhRvD, 102, 103010
Ding, M., Zhang, Y.-P., Zhang, Y.-J., et al. 2019, RAA, 19, 047
Driver, S. P., Norberg, P., Baldry, I. K., et al. 2009, A&G, 50, 5.12
Duffy, L. D., & van Bibber, K. 2009, NJPh, 11, 105008
Eisenstein, D. J., Zehavi, I., Hogg, D. W., et al. 2005, ApJ, 633, 560
Girelli, G., Pozzetti, L., Bolzonella, M., et al. 2020, A&A, 634, A135
Halenka, V., & Miller, C. J. 2020, PhRvD, 102, 084007
Heymans, C., Grocutt, E., Heavens, A., et al. 2013, MNRAS, 432, 2433
Heymans, C., Van Waerbeke, L., Miller, L., et al. 2012, MNRAS, 427, 146
Jungman, G., Kamionkowski, M., & Griest, K. 1996, PhR, 267, 195
Kang, K. J., Cheng, J. P., Chen, Y. H., et al. 2010, J. Phys. Conf. Ser., 203,
Kisslinger, L. S., & Das, D. 2019, IJMPA, 34, 1930013
Komatsu, E., Dunkley, J., Nolta, M. R., et al. 2009, ApJS, 180, 330
Kroupa, P. 2001, MNRAS, 322, 231
Kuijken, K., Heymans, C., Hildebrandt, H., et al. 2015, MNRAS, 454, 3500
Leauthaud, A., Saito, S., Hilbert, S., et al. 2017, MNRAS, 467, 3024
Luo, W., Yang, X., Lu, T., et al. 2018, ApJ, 862, 4
Luo, W., Yang, X., Zhang, J., et al. 2017, ApJ, 836, 38
Milgrom, M. 1983, ApJ, 270, 384
Milgrom, M. 2011, arXiv:1111.1611
Milgrom, M. 2013, PhRvL, 111, 041105
Milgrom, M. 2020, SHPMP, 71, 170
Navarro, J. F., Frenk, C. S., & White, S. D. M. 1997, ApJ, 490, 493
Nelson, D., Pillepich, A., Springel, V., et al. 2018, MNRAS, 475, 624
Perlmutter, S., Aldering, G., Goldhaber, G., et al. 1999, ApJ, 517, 565
Planck Collaboration, Ade, P. A. R., Aghanim, N., et al. 2016, A&A, 594, A13
Planck Collaboration, Aghanim, N., & Akrami, Y. 2020, A&A, 641, A6
Riess, A. G., Macri, L. M., Hoffmann, S. L., et al. 2016, ApJ, 826, 56
Shi, F., Yang, X., Wang, H., et al. 2018, ApJ, 861, 137
Sofue, Y., & Rubin, V. 2001, ARA&A, 39, 137
Verlinde, E. P. 2017, ScPP, 2, 016
Wong, K. C., Suyu, S. H., Chen, G. C. F., et al. 2020, MNRAS, 498, 1420
Yang, X., Mo, H. J., van den Bosch, F. C., et al. 2006, MNRAS, 373, 1159
Yang, X., Mo, H. J., van den Bosch, F. C., et al. 2007, ApJ, 671, 153
Yang, X., Mo, H. J., & van den Bosch, F. C. 2008, ApJ, 676, 248
Yang, X., Mo, H. J., van den Bosch, F. C., & Jing, Y. P. 2005, MNRAS,
  356, 1293
Yang, X., Xu, H., He, M., et al. 2021, ApJ, 909, 143
Zehavi, I., Blanton, M. R., Frieman, J. A., et al. 2002, ApJ, 571, 172
Zhang, H., Abdukerim, A., Chen, W., et al. 2019, SCPMA, 62, 31011
Zu, Y., & Mandelbaum, R. 2016, MNRAS, 457, 4360
ZuHone, J. A., & Sims, J. R. 2019, ApJ, 880, 145
Zwicky, F. 1937, ApJ, 86, 217
```